



Communication

Photocatalytic Degradation of Tobacco Tar Using CsPbBr₃ Quantum Dots Modified Bi₂WO₆ Composite Photocatalyst

Runda Huang¹, Menglong Zhang^{2,*}, Zhaoqiang Zheng¹, Kunqiang Wang³, Xiao Liu^{2,*} , Qizhan Chen¹ and Dongxiang Luo^{1,3,*}

¹ School of Materials and Energy, Guangdong University of Technology, Guangzhou 510006, China; 2111902118@mail2.gdut.edu.cn (R.H.); zhengzhq5@mail2.sysu.edu.cn (Z.Z.); qizanchen@gdut.edu.cn (Q.C.)

² Institute of Semiconductors, South China Normal University, Guangzhou 510631, China

³ School of Chemistry and Chemical Engineering, Institute of Clean Energy and Materials, Guangzhou Key Laboratory for Clean Energy and Materials, Huangpu Hydrogen Innovation Center, Guangzhou University, Guangzhou 510006, China; kunqiangwang@m.scnu.edu.cn

* Correspondence: mlzhang@m.scnu.edu.cn (M.Z.); liuxiao@m.scnu.edu.cn (X.L.); luodx@gdut.edu.cn (D.L.)

Abstract: Polycyclic aromatic hydrocarbons (PAHs) in tobacco tar are regarded as a significant threat to human health. PAHs are formed due to the incomplete combustion of organics in tobacco and cigarette paper. Herein, for the first time, we extended the application of CsPbBr₃ quantum dots (CsPbBr₃) to the photocatalytic degradation of tobacco tar, which was collected from used cigarette filters. To optimize the photoactivity, CsPbBr₃ was coupled with Bi₂WO₆ for the construction of a type-II photocatalyst. The photocatalytic performance of the CsPbBr₃/Bi₂WO₆ composite was evaluated by the degradation rate of PAHs from tobacco tar under simulated solar irradiation. The results revealed that CsPbBr₃/Bi₂WO₆ possesses a large specific surface area, outstanding absorption ability, good light absorption and rapid charge separation. As a result, in addition to good stability, the composite photocatalyst performed remarkably well in degrading PAHs (over 96% were removed in 50 mins of irradiation by AM 1.5 G). This study sheds light on promising novel applications of halide perovskite.

Keywords: nanocomposites; photocatalytic degradation; perovskite; tobacco tar



Citation: Huang, R.; Zhang, M.; Zheng, Z.; Wang, K.; Liu, X.; Chen, Q.; Luo, D. Photocatalytic Degradation of Tobacco Tar Using CsPbBr₃ Quantum Dots Modified Bi₂WO₆ Composite Photocatalyst. *Nanomaterials* **2021**, *11*, 2422. <https://doi.org/10.3390/nano11092422>

Academic Editors: Jihoon Lee, Ming-Yu Li and Antonino Gulino

Received: 20 July 2021

Accepted: 14 September 2021

Published: 17 September 2021

Publisher's Note: MDPI stays neutral with regard to jurisdictional claims in published maps and institutional affiliations.



Copyright: © 2021 by the authors. Licensee MDPI, Basel, Switzerland. This article is an open access article distributed under the terms and conditions of the Creative Commons Attribution (CC BY) license (<https://creativecommons.org/licenses/by/4.0/>).

1. Introduction

The development of economies can create problems such as energy shortages and environmental pollution, which are regarded as critical challenges to global sustainable development. In recent years, industrial and environmental pollution caused by organic pollutants has attracted considerable public attention [1,2]. In terms of human health, the main concerns include benzene compounds [3], formaldehyde [4], bacterial infections [5], and tobacco tar [6]. In particular, it is well known that tobacco tar is formed due to the incomplete combustion of organics in tobacco and cigarette paper. The substrates of tobacco are very complicated, and among these organic substrates, polycyclic aromatic hydrocarbons (PAHs) are considered as the major pollutants. This can be attributed to their bio-accumulative, toxic, carcinogenic, and recalcitrant features [7]. Thus, minimizing the toxicity of tobacco tar is desirable for human health and the environment. However, until now, not much research has been carried out on the degradation of tobacco tar via photocatalysis.

Among the techniques used for organic pollutant degradation, photocatalytic oxidation uses low-cost semiconductive materials and is considered as an environmentally-friendly path for the purification or transformation of organic pollutants [8–11]. Semiconductor-based photocatalytic reactions have already attracted extensive attention because they are a simple and environmentally friendly way to utilize solar energy. Therefore, numerous types of photocatalysts have been extensively investigated, such as TiO₂, ZnO, SnO₂, SrTiO₃,

LaFeO₃, BaTiO₃, and so on [12–17]. However, these semiconductors still have some common shortcomings, such as a narrow light absorption range and a high recombination ratio of photogenerated charges [18]. In this case, there is an urgent need to develop visible-light driven and highly active photocatalysts.

Bi₂WO₆ is currently regarded as a promising photocatalyst for its outstanding photo-redox ability, nontoxicity, and thermal and chemical stability [19]. Its potential applications include solar cells, photoelectrodes and photocatalysis [20–22]. However, the rapid recombination of excitonic pairs, ineffective charge separation and unsatisfactory visible-light absorption have limited the photocatalytic performance of pure Bi₂WO₆ [23]. Hence, different strategies have been applied to improve the photocatalytic properties of Bi₂WO₆, such as coupling with other semiconductors, morphological control, ion doping and surface modification [24–28]. One of the most accessible approaches is the deposition of quantum dots (QDs) onto the semiconductor surface, which is beneficial due to their noteworthy properties, including high charge separation efficiency and quantum confinement effects [29,30]. Thus, modification with QDs is regarded as an effective method to improve the photocatalytic performance of semiconductor materials.

Among the various QDs materials, CsPbBr₃ QDs have received increasing interest due to their high luminescent quantum yields [31] in solid states in the green range (band gap energy = 2.4 eV) and superior environmental stability in comparison to other perovskites with organic cations [32]. Perovskite materials possess unique advantages in regard to effective charge separation and electron hole diffusion, which makes them suitable not only for the photovoltaic field, but also for several photocatalytic reaction types [33,34]. In addition, CsPbBr₃ is very attractive due to its high thermal-stability and photo-resistance [35]. Considering these advantages, CsPbBr₃ was used to decorate Bi₂WO₆ via a hydrothermal method in this work and the photoactivity was evaluated through the photocatalytic degradation of PAHs in tobacco tar under simulated solar light. Additionally, the CsPbBr₃/Bi₂WO₆ heterogeneous photocatalyst exhibited increased specific surface area and improved light absorption in the visible range, which effectively promoted the photocatalytic activity [36]. Compared with pure Bi₂WO₆, the CsPbBr₃/Bi₂WO₆ composites exhibit superior photocatalytic activity and stability. This work presents a promising strategy for designing a more efficient composite photocatalyst-based semiconductor photocatalyst for application to pollutant purification. In addition, to the best of our knowledge, this work is the first to utilize perovskite for the degradation of PAHs.

2. Experimental Section

2.1. Reagents and Materials

Bismuth nitrate pentahydrate (Bi(NO₃)₃·5H₂O, 99%), ethanol (CH₃CH₂OH, 99.7%), nitric acid (HNO₃, 68%), sodium tungstate dehydrates (Na₂WO₄·2H₂O, 99.5%) were purchased from Aladdin Industrial Co, Ltd. (Shanghai, China) and CsPbBr₃ perovskite QDs was purchased from Nanjing MKNANO, China and used as received. The used cigarette filters were collected randomly. The deionized water used throughout all experiments was purified through a Millipore system (Millipore, Billerica, MA, USA).

2.2. Synthesis of CsPbBr₃/Bi₂WO₆

Pure Bi₂WO₆ was synthesized via a hydrothermal method. First, Bi(NO₃)₃·5H₂O (1 mmol) was dissolved in an aqueous solvent mixture of 30 mL HNO₃ (pH = 3) and 20 mL Na₂WO₄·2H₂O (0.5 mmol). The mixed solution was then vigorously stirred until clear, under room temperature. The solution was subsequently heat-treated in a muffle furnace at 120 °C for 2 h. The resultant precipitate was dried to obtain the pure Bi₂WO₆ photocatalyst (light-yellow powder). Subsequently, 1 mL of CsPbBr₃ suspension (10 mg/mL, purchased from Nanjing MKNANO, Nanjing, China) was ultrasonicated for 30 min to generate CsPbBr₃ QDs dispersion. Then, a certain amount of Bi₂WO₆ was added into the above CsPbBr₃ suspension and stirred for 20 h. For example, to prepared 10 wt% CsPbBr₃/Bi₂WO₆, 90 mg of Bi₂WO₆ was added to the 1 mL suspension. Subsequently, the

mixture was evaporated at 40 °C for 10 h and the composite photocatalyst was obtained after drying.

2.3. Photocatalytic Experiments

The tobacco tar was obtained by immersing 10 randomly collected used cigarette filters in 50 mL trifluorotoluene, followed by 10 min ultra-sonification to give a brown-yellow tobacco tar solution. The cigarette filters were then removed from the solution. The concentrations of the substrates in the tobacco tar solution were confirmed using gas chromatography (GC). The as-prepared photocatalyst was uniformly dispersed in 2 mL of tobacco tar solution with 20 min ultrasonic treatment. Then, the samples were illuminated by Xe lamp with an AM 1.5 G filter as the simulated solar source. The photoactivity was confirmed by monitoring the concentrations of PAHs under different illumination time.

2.4. Characterization

The crystal structure of the samples was studied by X-ray diffractometry (XRD; Bruker-AXS D8 Advance, Karlsruhe, Germany). Field emission scanning electron microscopy (SEM) (Hitachi S-4800, Tokyo, Japan) and transmission electron microscopy (TEM) (JEOL JEM-2100, Tokyo, Japan) were performed for the morphological and microstructural analyses, respectively, of the samples. The UV-vis absorption spectroscopy of the samples was performed by a UV-vis near-infrared spectrophotometer (Agilent Cary 5000, Palo Alto, CA, USA). The XPS energy spectrum was determined by an X-ray photoelectron spectrometer (Thermo Fisher/Escalab 250Xi, Waltham, MA, USA). Measuring the surface area and pore size distribution of samples was performed using a specific surface and porosity analyzer (Micromeritics ASAP2460, Atlanta, GA, USA). TGA analysis was done by using the Mettler Toledo TGA/DSC 3+ instrument (Zurich, Switzerland). Total organic carbon (TOC) content in solvent was assessed by a TOC analyzer (Shimadzu, TOC-L-VCPN, Tokyo, Japan). The photocatalytic result was characterized by single quadrupole gas chromatography-mass spectrometry (Thermo Fisher/Trace1300 ISQ QD, Waltham, MA, USA).

3. Results and Discussion

3.1. Properties of the Composite Photocatalysts

Powder X-ray diffraction (PXRD) (Figure 1a) was initially exploited to evaluate the phase and crystallinity of the as-prepared CsPbBr₃ QDs-decorated Bi₂WO₆ (CsPbBr₃/Bi₂WO₆). A p-FTO glass slide was used as a substrate to support the samples for characterization. The main peaks at 2θ of 28.3°, 32.8°, 47.0°, 55.8° and 58.5° can be indexed to an orthorhombic Bi₂WO₆ (JCPDS#39-0256), and corresponded to the indices of (131), (200), (260), (331) and (262) planes, respectively. On the other hand, the diffraction patterns of cubic CsPbBr₃ corresponded to JCPDS#54-0752 and a previous report [32,37]. The transmission electron microscopy (TEM, Figure 1b) revealed that the CsPbBr₃ QDs of a few nanometers were dispersed on Bi₂WO₆ with a quasi-rectangle morphology. The two materials were subsequently confirmed by high-resolution transmission electron microscopy (HR-TEM), which showed the lattice spacing of CsPbBr₃ ([220] = 0.20 nm) and Bi₂WO₆ ([200] = 0.28) (Figure 1d), which can be compared to the diffraction results from PXRD. In addition, as illustrated in Figure 1c, the connected boundary presented as a semi-coherent interface involving several unit cells. The lattice mismatch between the crystal planes of these two components can be defined as $\Delta d/d_{\text{Bi}_2\text{WO}_6} = 28\%$. Furthermore, as shown in Figure 1c,d, CsPbBr₃ and Bi₂WO₆ exhibited periodically coincided lattice (7d (CsPbBr₃) = 5d (Bi₂WO₆)), suggesting that intimate energetic and chemical interactions were formed at the semi-coherent interface of the two components [38].

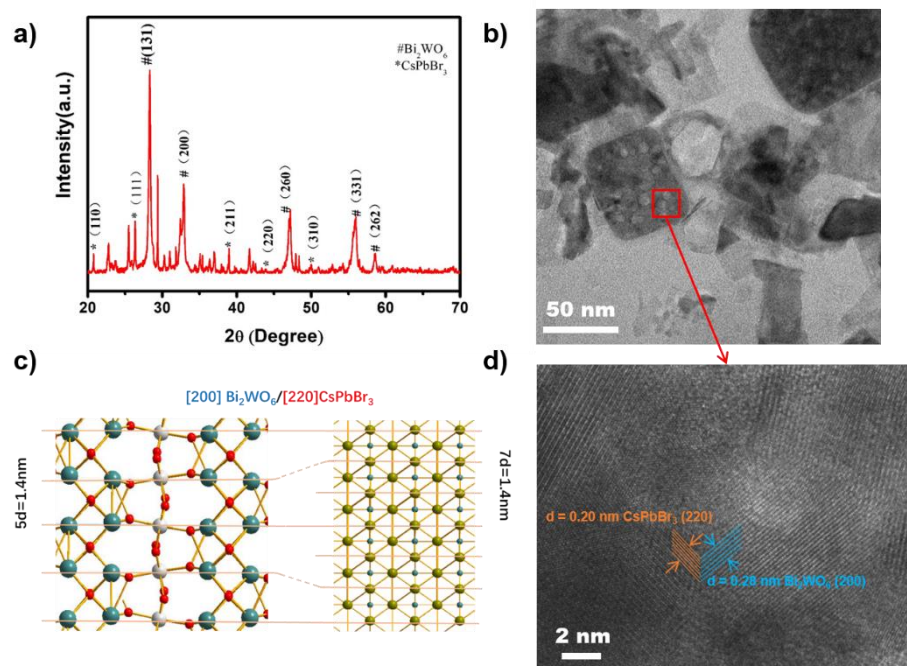


Figure 1. (a) PXRD patterns and (b) TEM image of the as-prepared 15 wt% CsPbBr₃/Bi₂WO₆ photocatalyst; (c) schematic diagram of semi-coherent interface of the two components; (d) HR-TEM image of the as-prepared 15 wt% CsPbBr₃/Bi₂WO₆ photocatalyst.

The elemental composition of the as-prepared pure Bi₂WO₆ and CsPbBr₃/Bi₂WO₆ were confirmed by X-ray photoelectron spectroscopy (XPS), which demonstrated that the CsPbBr₃/Bi₂WO₆ sample contained no other elements apart from O, Bi, Cs, Pb, Br, C 1 and W (Figure 2a). The surface atomic content was calculated by the fitting peak area and sensitivity factor, as shown in Table 1 (the carbon atomic content comes from the XPS instrument). Besides, the altered chemical state of the coupled materials was recorded by XPS as well; as shown in Figure 2b–d, the characteristic peaks of W4f_{5/2} and W4f_{7/2} in pristine CsPbBr₃/Bi₂WO₆ were located at 37.8 and 35.7 eV (Figure 2b), the characteristic peaks of Bi4f_{5/2} and Bi4f_{7/2} were located at 164.8 and 159.3 eV (Figure 2c), and the characteristic peaks of O1s were located at 533.3, 532.0 and 530.4 eV (Figure 2d). In the Bi₂WO₆ sample, the characteristic peaks of W4f_{5/2} and W4f_{7/2} were located at 37.4 and 35.3 eV (Figure 2b), the characteristic peaks of Bi4f_{5/2} and Bi4f_{7/2} were located at 164.4 and 158.9 eV (Figure 2c), and the characteristic peak of O1s was 533.4, 532.1 and 530.2 eV (Figure 2d). This showed that the valence state of Bi, W and O in the composite sample was +3, +6 and −2, respectively. In comparison to pristine Bi₂WO₆, the binding energy of Bi4f, W4f in the CsPbBr₃/Bi₂WO₆ samples shifted ca. 0.7 and 0.4 towards the higher energy, respectively. This could be attributed to the regional environment and electron density change of Bi₂WO₆ and CsPbBr₃ in the composites due to strong heterojunction formation [39]. In detail, the Bi₂WO₆ displayed increased electron accepting capacity and decreased electron density. On the other hand, this is accompanied by an increase in the electron density and an improvement in the electron-donating capacity on the CsPbBr₃ side. Consequently, the internal electric field was established, leading to a tendency for electron transfer from CsPbBr₃ to Bi₂WO₆, and as a result, a typical type-II band structure was formed.

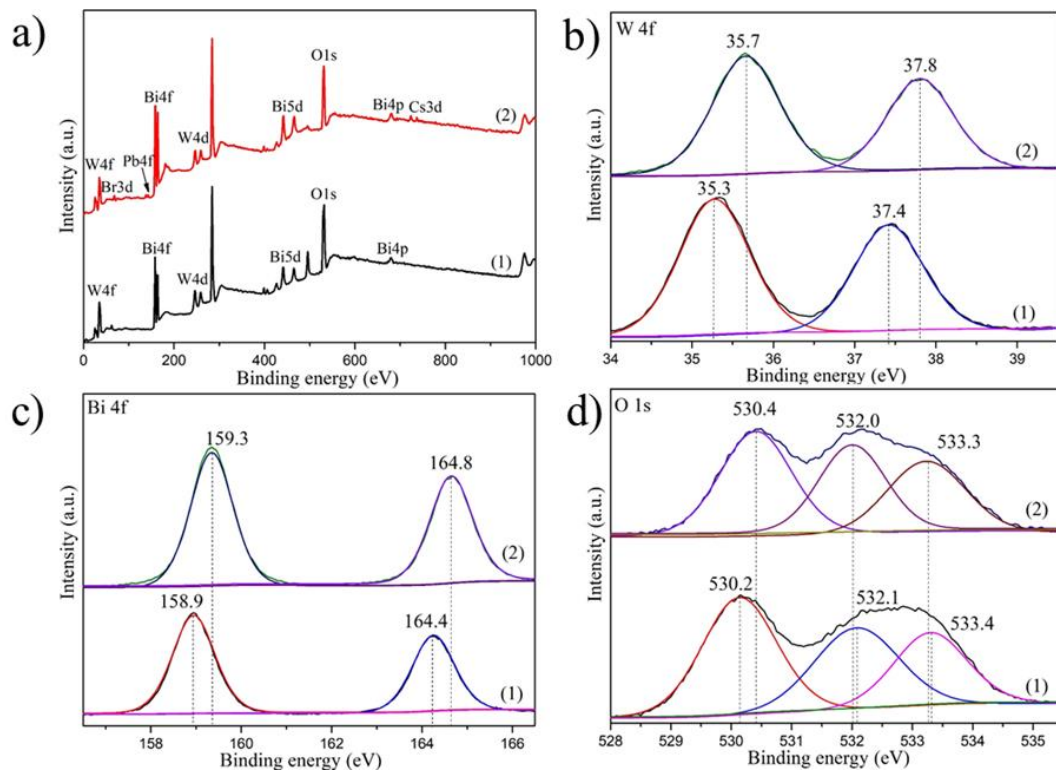


Figure 2. XPS spectra of (1) pure Bi_2WO_6 and (2) 15 wt% $\text{CsPbBr}_3/\text{Bi}_2\text{WO}_6$ samples. (a) Survey scan; (b) W4f; (c) Bi4f; (d) O1s.

Table 1. Relative atomic content of pure Bi_2WO_6 and 15 wt% $\text{CsPbBr}_3/\text{Bi}_2\text{WO}_6$ samples.

Sample	Bi4f/%	W4f/%	O1s/%	C1s/%	Br3d/%	Pb4f/%	Cs4d/%
Bi_2WO_6	1.62	2.53	24.04	71.8	0	0	0
$\text{CsPbBr}_3/\text{Bi}_2\text{WO}_6$	2.21	2.15	21.7	72.74	0.96	0.09	0.16

In order to explore the electronic features of $\text{CsPbBr}_3/\text{Bi}_2\text{WO}_6$, Hall effect measurement was employed to monitor the charge carrier density and the Hall mobility. Hall effect measurement is an important approach for investigating the charge transport mechanisms in Bi_2WO_6 with or without the coupling of CsPbBr_3 QDs. Here, as shown in Table 2, the Bi_2WO_6 sample exhibited lower charge carrier density ($2.738 \times 10^{11} \text{ cm}^{-3}$) than that of $\text{CsPbBr}_3/\text{Bi}_2\text{WO}_6$ ($5.154 \times 10^{14} \text{ cm}^{-3}$). In contrast to the reduced charge density in the Z-scheme due to the recombination of electrons and holes between the two component materials, this result was consistent with the type-II feature of the composite materials, which possessed accumulated charges. Meanwhile, greater mobility was observed from pristine Bi_2WO_6 in comparison to that of $\text{CsPbBr}_3/\text{Bi}_2\text{WO}_6$; this can be attributed to the effective mass of the carriers. According to the equation: $\mu = \frac{\tau e}{m}$, the mobility (μ) is proportional to the elemental charge (e) and carrier mean free time (τ). In contrast, the mobility is inversely proportional to the effective mass of the carriers (m), and a greater m typically indicates larger carrier density [40].

Table 2. Hall effect measurement of pure Bi_2WO_6 and 15 wt% $\text{CsPbBr}_3/\text{Bi}_2\text{WO}_6$ samples.

Sample	Carrier Density (cm^{-3})	Hall Mobility ($\text{cm}^2\text{V}^{-1}\text{s}^{-1}$)	p/n Type
Bi_2WO_6	2.738×10^{11}	25.316	n
$\text{CsPbBr}_3/\text{Bi}_2\text{WO}_6$	5.154×10^{14}	4.672	p

The morphologies of the as-prepared samples were confirmed by scanning electron microscopy (SEM). The Bi_2WO_6 displayed particles of a few hundred nanometers with exposed flat and smooth facets as shown in Figure 3a. In comparison to the pure Bi_2WO_6 , the as-prepared $\text{CsPbBr}_3/\text{Bi}_2\text{WO}_6$ composite exhibited a rougher morphology due to the decoration of CsPbBr_3 dots on the facets of Bi_2WO_6 (Figure 3b). These SEM results were consistent with the cubic-shaped particles on the micro-square observed by TEM under low magnification (Figure 1b). The rough morphologies of the composite material lead to efficient light absorption due to their light trapping effect [41]. Besides, the surface area could be increased due to the presence of CsPbBr_3 quantum dots on Bi_2WO_6 , which was confirmed by N_2 adsorption-desorption isotherms. The samples presented typical Type-IV adsorption isotherms with a H_3 hysteresis loop (Figure S1a), illustrating the porous nature of the catalysts [42]. Furthermore, the specific surface area of the Bi_2WO_6 and $\text{CsPbBr}_3/\text{Bi}_2\text{WO}_6$ were compared and $\text{CsPbBr}_3/\text{Bi}_2\text{WO}_6$ exhibited a more than 4-fold larger surface area than that of Bi_2WO_6 . The details of the isotherm studies can be found in Table 3. The high surface area of $\text{CsPbBr}_3/\text{Bi}_2\text{WO}_6$ suggested an improvement in the active sites and adsorption capacity, which allows rapid interaction with the reactants. Next, the pure Bi_2WO_6 and $\text{CsPbBr}_3/\text{Bi}_2\text{WO}_6$ were subjected to thermal gravimetric analysis (TGA) using -temperatures ranging from room temperature to 600 °C with a heat rate of 5 °C/min in fluid He (20 mL/min). As illustrated in Figure S1b, $\text{CsPbBr}_3/\text{Bi}_2\text{WO}_6$ exhibited improved thermal stability in comparison to the pure Bi_2WO_6 , especially from 250 °C to 600 °C. This could be attributed to the strong interaction between CsPbBr_3 and Bi_2WO_6 .

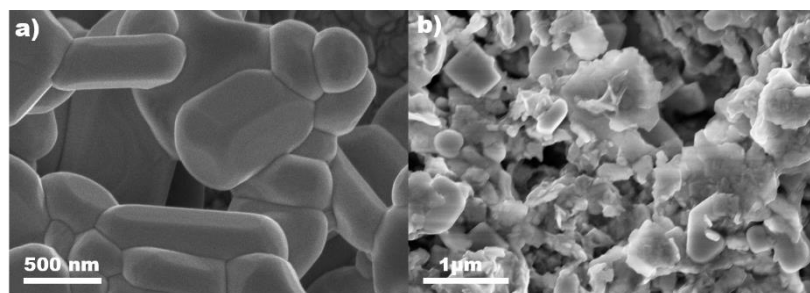


Figure 3. SEM images of (a) Bi_2WO_6 and (b) $\text{CsPbBr}_3/\text{Bi}_2\text{WO}_6$ photocatalysts.

Table 3. The specific surface of Bi_2WO_6 and $\text{CsPbBr}_3/\text{Bi}_2\text{WO}_6$.

Catalyst	BET Surface Area (m^2/g)	t-Plot External Surface Area (m^2/g)
$\text{CsPbBr}_3/\text{Bi}_2\text{WO}_6$	9.88	9.70
Bi_2WO_6	5.04	5.34

In Figure 4a, the UV-vis absorption spectra of pure Bi_2WO_6 and the $\text{CsPbBr}_3/\text{Bi}_2\text{WO}_6$ composite are illustrated. The pure Bi_2WO_6 presented an absorption edge at ca. 445 nm, corresponding to its typical band gap energy of 2.78 eV. After loading with CsPbBr_3 QDs, a dramatically enhanced absorption below ca. 510 nm was observed, which indicated the optimized light harvesting capacity of the composite photocatalyst [38,43–45]. In addition, as presented in Figure 4b, a decreased intensity and slightly blue-shift in the photoluminescence (PL) peak was observed when coupling the CsPbBr_3 with Bi_2WO_6 , which indicated that the recombination rate of electron-hole pairs were suppressed, and thus they promote the photocatalytic efficiency [46].

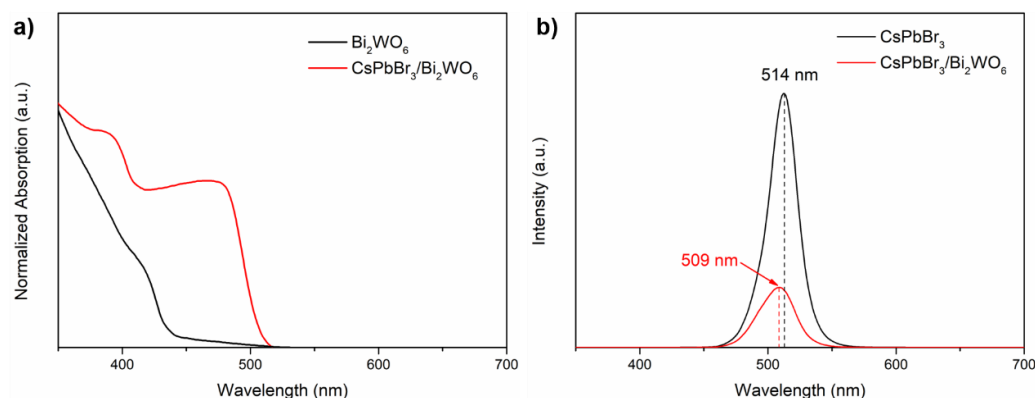


Figure 4. (a) UV-vis absorption spectra and (b) steady-state PL spectra of CsPbBr₃ and 15 wt% CsPbBr₃/Bi₂WO₆.

3.2. Activity for Photodegradation of PAHs from Tobacco Tar

Trifluorotoluene was employed as the solvent to dissolve the tobacco tar due to its apolar nature, good solubility, and superior chemical stability comparing with toluene. A list of the main substrates in the tobacco tar solution identified by gas chromatography-mass spectrometry (GC-MS) is given in Table S1. A Xe lamp (100 mW cm⁻²) coupled with AM 1.5 G filters were utilized as the simulated solar source for illumination. GC-MS and UV-visible absorption spectra (UVAS) were exploited to evaluate the products and degradation rate of the photocatalysts. A series of tests was carried out under room temperature, and the photocatalytic reactor was saturated with different matter (air, H₂O, and O₂) to investigate the key radicals for promoting the degradation rate. To reach adsorption equilibrium, the as-prepared photocatalysts were initially mixed with tobacco tar under stirring (1200 rpm) in the dark for 30 min prior to the photocatalytic reactions.

As reported previously [47,48], the highly reactive hydroxyl radicals ($\cdot\text{OH}$) and superoxide radicals ($\cdot\text{O}_2^-$) formed in the photocatalytic process are desirable for degrading PAHs into less toxic products. Thus, the samples were saturated with air to supply the source H₂O and O₂ needed to accelerate the generation of hydroxyl and superoxide radicals. As shown in Figure 5, approximately 32% of the PAHs was degraded with the pure Bi₂WO₆ photocatalyst in 50 min. This can be compared to the CsPbBr₃/Bi₂WO₆ composite, which presented a significantly improved degradation rate. This can be attributed to the efficient charge separation of the type-II band structure and the enhanced light absorption of the CsPbBr₃. In addition, the degradation rate was systematically enhanced with the increasing weight ratio of the CsPbBr₃ in the composites (Figure S2), and reached its maximum at 96% when loaded with 15 wt% CsPbBr₃ (Figure 5a,b). The total organic carbon (TOC) content in the solvent was assessed by a TOC analyzer to further reflect the degree of PAHs degradation. As shown in Table S2, the TOC content in the reaction system decreased from 5.36 mg/L before the reaction to 2.3 mg/L after the reaction, indicating that the CsPbBr₃/Bi₂WO₆ composite photocatalyst is ideal for mineralizing PAHs. The products mainly consisted of monocyclic aromatic hydrocarbons with low toxicity and carbon oxide, as listed in Table S3. Although increasing the ratio of CsPbBr₃ in the composites enhances the light absorption due to the outstanding light harvesting capacity of perovskite, overloading leads to aggregations resulting in a longer migration pathway for photogenerated charges. In addition, the overloading might also reduce the exposed surface area of Bi₂WO₆ to reactants. Consequently, increasing the perovskite ratio further is not necessary to optimize the degradation rate. To the best of our knowledge, there is no previous research on the photocatalytic degradation of PAHs in tobacco tar. Thus, we compared our optimal sample (over 96% degradation in 50 min) with that for PAH removal in water treatment, such as TiO₂ (over 99% in 24 h) [49], ZnO/TiO₂ (98% in 2 h) [50], TiO₂ (over 66% in 39 min) [51], Evonik P25 (70% in 8 h) [52] and Pr/TiO₂ (over 99% in 3 h) [53].

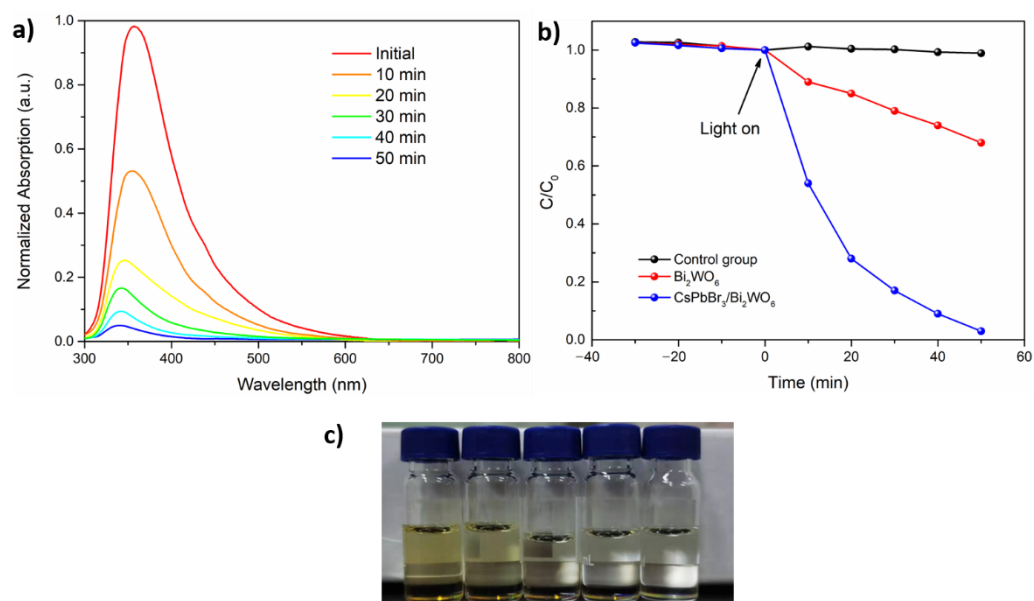


Figure 5. (a) The absorption spectra of the samples using 15 wt% CsPbBr₃/Bi₂WO₆ as a photocatalyst for different times; (b) photocatalytic degradation of tobacco tar using pure Bi₂WO₆, 15 wt% CsPbBr₃/Bi₂WO₆ and control group (without photocatalyst); (c) digital photographs of the sample using 15 wt% CsPbBr₃/Bi₂WO₆ as a photocatalyst for 10 to 50 min (from left to right). Reaction condition: 50 mg photocatalyst, saturated with air, stirred in the dark for 30 min before experiments; then, the reactions were conducted under AM 1.5 G simulated light irradiation for 50 min.

To investigate the photodegradation process, electron paramagnetic resonance (EPR) spectra were employed to confirm the generated reactive radicals under simulated solar light. The EPR signals of hydroxyl and superoxide radicals (Figure 6a) were recorded [38,54,55] after illumination for 5 min as these two radicals are typically considered responsible for the high degradation rate of PAHs. Control experiments were carried out to confirm the respective influence of these radicals on the photodegradation. To this end, one sample was degassed by Ar and then saturated with O₂ to eliminate the source of hydroxyl generation, another sample was degassed with Ar and then 20 μL H₂O was added to inhibit the superoxide generation. Compared to the sample saturated with air, the degradation rate dramatically reduced in the absence of a source for hydroxyl generation (Figure 6b). In contrast, the sample showed a dramatically decreased degradation rate when the source of superoxide radicals was excluded. These results suggested that the hydroxyl radicals with oxidation reactivity were predominant in the degradation of PHAs, and degradation benefits from the presence of water and oxygen. Aside from photocatalytic activity, the stability of a photocatalyst is an important criterion. As shown in Figure S3, the photocatalytic activity only decreased by 7% after six consecutive cycles, suggesting that CsPbBr₃/Bi₂WO₆ photocatalyst has high stability and reusability. The XRD spectra in Figure S4 shows that the diffraction peaks of the material's crystal structure did not change significantly after six cycles. In addition, no trace of Pd ions was found after the reaction, which can be attributed to the stable nature of CsPbBr₃ in apolar solvent.

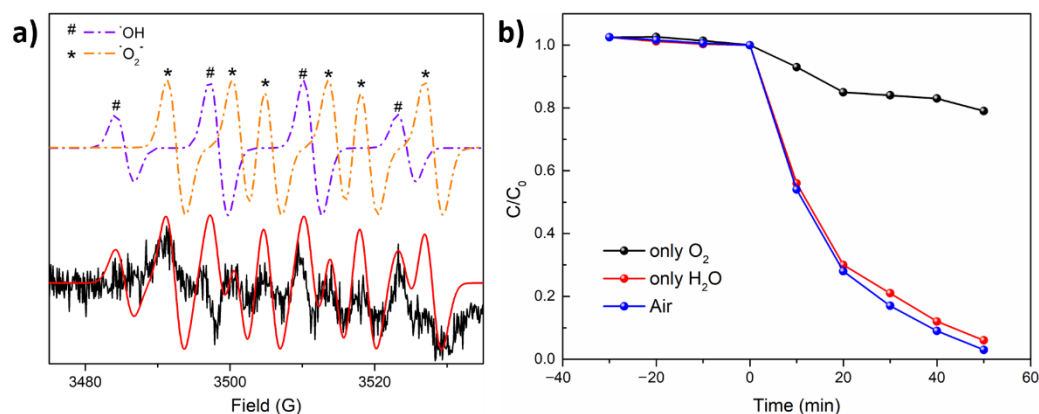


Figure 6. (a) EPR spectra of CsPbBr₃/Bi₂WO₆ sample saturated with air under illumination for 5 min and 5,5-dimethyl-pyrroline N-oxide (DMPO) was used as trap agent; (b) photocatalytic degradation rate of 15 wt% CsPbBr₃/Bi₂WO₆ sample when saturated with different gases.

4. Photocatalytic Mechanism

Based on the Tauc plots shown in Figure S5a,b, the band gap energy (E_g) of the Bi₂WO₆ and CsPbBr₃ samples were measured to be 2.71 eV, and 2.39 eV from the linear part of the $(\alpha h\nu)^2 - (h\nu)$ curves. The VB values (E_{VB}) and CB values (E_{CB}) for a semiconductor can be calculated according to the following equations:

$$E_{CB} = E_{VB} - E_g \quad (1)$$

$$E_{VB} = \chi - E_e + 0.5E_g \quad (2)$$

The electronegativity (χ) of Bi₂WO₆ and CsPbBr₃ is 6.36 eV and 4.38 eV, respectively, according to previous reports [56,57]. E_e was 4.5 eV, which is the energy of free electrons on a hydrogen atom. Thus, we can conclude that the E_{VB} of Bi₂WO₆ and CsPbBr₃ was 3.25 and 1.075 eV while their associated E_{CB} was 0.505 eV and -1.315 eV, respectively, versus normal hydrogen electrode (NHE). On the basis of the above results, a possible photocatalytic mechanism for degradation of PAHs was proposed (Figure 7). The type II heterojunction was formed at the interfaces between CsPbBr₃ and Bi₂WO₆. Under illumination, both CsPbBr₃ and Bi₂WO₆ were excited to produce photogenerated electrons and holes. Then, to achieve Fermi level balance, the conduction electrons of CsPbBr₃ were transferred to the conduction band of Bi₂WO₆ under the potential difference of the band energy. At the same time, the valence holes of Bi₂WO₆ were transferred to the VB of CsPbBr₃. Finally, both CsPbBr₃ and Bi₂WO₆ have improved charge separation efficiency, and hence increased activity for oxidation and reduction, respectively. The reserved holes can oxidize water molecules or hydroxyl ions to produce hydroxyl radicals. Meanwhile, the reserved electrons can reduce O₂ to yield superoxide radicals. Finally, according to the EPR spectra results, PAHs were degraded into octopamine, carbon dioxide, toluene and other substances under the joint action of superoxide and hydroxyl radicals. Of the two active radicals, hydroxyl radicals were predominant in the photocatalytic reaction.

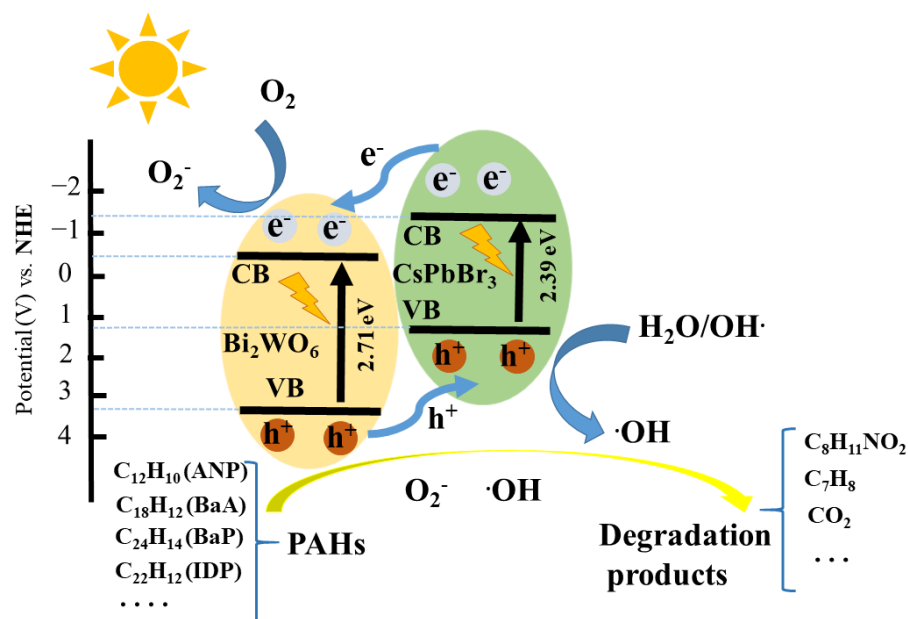


Figure 7. Schematic photocatalytic reaction process and charge transfer of the CsPbBr₃/Bi₂WO₆ composite catalyst under solar light irradiation.

5. Conclusions

In this research, CsPbBr₃ QDs decorated Bi₂WO₆ was successfully prepared by using a hydrothermal method. The sample was used as a photocatalyst to investigate its novel application for photodegradation of tobacco tar under visible radiation. The CsPbBr₃/Bi₂WO₆ presented outstanding activity compared to classic metal oxides catalysts, and the degradation products were mainly low toxic compounds. The findings of this work may open a promising avenue for producing high-efficiency photocatalysts with special heterostructures for removing organic contaminants from used tobacco tar, and could potentially be applied to novel cigarette filters in the future.

Supplementary Materials: The following are available online at <https://www.mdpi.com/article/10.3390/nano11092422/s1>, Figure S1. (a) adsorption/desorption isotherms of pure Bi₂WO₆ and CsPbBr₃/Bi₂WO₆; (b) the TGA curves of pure Bi₂WO₆ and CsPbBr₃/Bi₂WO₆; Figure S2. Degradation rate of PAHs using 15 wt% CsPbBr₃/Bi₂WO₆ composite photocatalyst with different CsPbBr₃ weight ratios; Figure S3. Degradation rate of PAHs using 15 wt% CsPbBr₃/Bi₂WO₆ composite photocatalyst with air in different reaction cycles; Figure S4. XRD patterns of 15 wt% CsPbBr₃/Bi₂WO₆ before reaction and after six reactions; Figure S5. Tauc plots of the Bi₂WO₆ (a) and CsPbBr₃ (b); Table S1. The total organic carbon (TOC) content of PAHs with 15 wt% CsPbBr₃/Bi₂WO₆ nanocomposite; Table S2. The main substrates from tobacco tar identified by GC-MS; Table S3. The main products from the photodegradation of tobacco tar. Noted that there are side-products with low concentration.

Author Contributions: Conceptualization, D.L. and M.Z.; methodology, R.H. and Q.C.; software, K.W.; validation, X.L.; formal analysis, R.H.; investigation, X.L.; resources, D.L.; data curation, Z.Z.; writing—original draft preparation, R.H. and M.Z.; writing—review and editing, M.Z. and D.L.; visualization, R.H.; supervision, D.L.; project administration, M.Z.; funding acquisition, D.L. All authors have read and agreed to the published version of the manuscript.

Funding: The authors are grateful to the Science and Technology Program of Guangzhou (202103030001), Guangdong Basic and Applied Basic Research Foundation (Grant No. 2020B1515020032), the National Natural Science Foundation of China (Grant No. 62074060), the Guangdong Basic and Applied Basic Research Foundation (Grant No. 2020B1515120022) and the Guangdong Science and Technology Plan (Grant No. 2019B040403003).

Institutional Review Board Statement: Not applicable.

Informed Consent Statement: Not applicable.

Data Availability Statement: Not applicable.

Acknowledgments: The authors thank Weizhe Wang for proceeding the EPR data.

Conflicts of Interest: The authors declare no conflict of interest.

References

1. Singh, J.; Kumar, V.; Jolly, S.S.; Kim, K.-H.; Rawat, M.; Kukkar, D.; Tsang, Y.F. Biogenic synthesis of silver nanoparticles and its photocatalytic applications for removal of organic pollutants in water. *J. Ind. Eng. Chem.* **2019**, *80*, 247–257. [[CrossRef](#)]
2. Soltan, W.B.; Ammar, S.; Olivier, C.; Toupance, T. Influence of zinc doping on the photocatalytic activity of nanocrystalline SnO₂ particles synthesized by the polyol method for enhanced degradation of organic dyes. *J. Alloys Compd.* **2017**, *729*, 638–647. [[CrossRef](#)]
3. Andreoli, R.; Spatari, G.; Pignini, D.; Poli, D.; Banda, I.; Goldoni, M.; Riccelli, M.G.; Petyx, M.; Protano, C.; Vitali, M.; et al. Urinary biomarkers of exposure and of oxidative damage in children exposed to low airborne concentrations of benzene. *Environ. Res.* **2015**, *142*, 264–272. [[CrossRef](#)]
4. Yan, Z.; Xu, Z.; Yu, J.; Jaroniec, M. Enhanced formaldehyde oxidation on CeO₂/AlOOH-supported Pt catalyst at room temperature. *Appl. Catal. B Environ.* **2016**, *199*, 458–465. [[CrossRef](#)]
5. Husman, T. Health effects of indoor-air microorganisms. *Scand. J. Work Environ. Health* **1996**, *22*, 5–13. [[CrossRef](#)]
6. Alexandrov, L.B.; Ju, Y.S.; Haase, K.; Van Loo, P.; Martincorena, I.; Nik-Zainal, S.; Totoki, Y.; Fujimoto, A.; Nakagawa, H.; Shibata, T.; et al. Mutational signatures associated with tobacco smoking in human cancer. *Science* **2016**, *354*, 618–622. [[CrossRef](#)]
7. Enguita, F.J.; Leitao, A.L. Hydroquinone: Environmental pollution, toxicity, and microbial answers. *BioMed Res. Int.* **2013**, *2013*, 542168. [[CrossRef](#)]
8. Chen, X.; Sun, H.; Zelekew, O.A.; Zhang, J.; Guo, Y.; Zeng, A.; Kuo, D.-H.; Lin, J. Biological renewable hemicellulose-template for synthesis of visible light responsive sulfur-doped TiO₂ for photocatalytic oxidation of toxic organic and As(III) pollutants. *Appl. Surf. Sci.* **2020**, *525*, 146531. [[CrossRef](#)]
9. Nagajyothi, P.; Vattikuti, S.; Devarayapalli, K.; Yoo, K.; Shim, J.; Sreekanth, T. Green synthesis: Photocatalytic degradation of textile dyes using metal and metal oxide nanoparticles-latest trends and advancements. *Crit. Rev. Environ. Sci. Technol.* **2019**, *50*, 2617–2723. [[CrossRef](#)]
10. Liu, Y.; Li, M.; Zhang, Q.; Qin, P.; Wang, X.; He, G.; Li, L. One-step synthesis of a WO₃-CuS nanosheet heterojunction with enhanced photocatalytic performance for methylene blue degradation and Cr(VI) reduction. *J. Chem. Technol. Biotechnol.* **2019**, *95*, 665–674. [[CrossRef](#)]
11. Thirukumaran, P.; Atchudan, R.; Parveen, A.S.; Kalaiarasan, K.; Lee, Y.R.; Kim, S.-C. Fabrication of ZnO nanoparticles adorned nitrogen-doped carbon balls and their application in photodegradation of organic dyes. *Sci. Rep.* **2019**, *9*, 19509. [[CrossRef](#)] [[PubMed](#)]
12. He, F.; Muliane, U.; Weon, S.; Choi, W. Substrate-specific mineralization and deactivation behaviors of TiO₂ as an air-cleaning photocatalyst. *Appl. Catal. B Environ.* **2020**, *275*, 119145. [[CrossRef](#)]
13. Wang, H.; Qiu, X.; Liu, W.; Yang, D. Facile preparation of well-combined lignin-based carbon/ZnO hybrid composite with excellent photocatalytic activity. *Appl. Surf. Sci.* **2017**, *426*, 206–216. [[CrossRef](#)]
14. Ullah, I.; Munir, A.; Muhammad, S.; Ali, S.; Khalid, N.; Zubair, M.; Sirajuddin, M.; Hussain, S.Z.; Ahmed, S.; Khan, Y.; et al. Influence of W-doping on the optical and electrical properties of SnO₂ towards photocatalytic detoxification and electrocatalytic water splitting. *J. Alloys Compd.* **2020**, *827*, 154247. [[CrossRef](#)]
15. Parida, K.M.; Reddy, K.H.; Martha, S.; Das, D.P.; Biswal, N. Fabrication of nanocrystalline LaFeO₃: An efficient sol-gel auto-combustion assisted visible light responsive photocatalyst for water decomposition. *Int. J. Hydrogen Energy* **2010**, *35*, 12161–12168. [[CrossRef](#)]
16. Yadav, A.A.; Hunge, Y.M.; Mathe, V.L.; Kulkarni, S.B. Photocatalytic degradation of salicylic acid using BaTiO₃ photocatalyst under ultraviolet light illumination. *J. Mater. Sci. Mater. Electron.* **2018**, *29*, 15069–15073. [[CrossRef](#)]
17. Zhang, G.; Liu, G.; Wang, L.; Irvine, J.T.S. Inorganic perovskite photocatalysts for solar energy utilization. *Chem. Soc. Rev.* **2016**, *45*, 5951–5984. [[CrossRef](#)]
18. Xie, T.; Liu, Y.; Wang, H.; Wu, Z. Synthesis of α -Fe₂O₃/Bi₂WO₆ layered heterojunctions by in situ growth strategy with enhanced visible-light photocatalytic activity. *Sci. Rep.* **2019**, *9*, 7551. [[CrossRef](#)]
19. Dumrongrojthanath, P.; Phuruangrat, A.; Thongtem, S.; Thongtem, T. Hydrothermal preparation of visible-light-driven Br-doped Bi₂WO₆ photocatalyst. *Mater. Lett.* **2017**, *209*, 501–504. [[CrossRef](#)]
20. Zhang, P.; Teng, X.; Feng, X.; Ding, S.; Zhang, G. Preparation of Bi₂WO₆ photocatalyst by high-energy ball milled Bi₂O₃-WO₃ mixture. *Ceram. Int.* **2016**, *42*, 16749–16757. [[CrossRef](#)]
21. Kaur, A.; Kansal, S.K. Bi₂WO₆ nanocuboids: An efficient visible light active photocatalyst for the degradation of levofloxacin drug in aqueous phase. *Chem. Eng. J.* **2016**, *302*, 194–203. [[CrossRef](#)]
22. Zhuo, Y.; Huang, J.; Cao, L.; Ouyang, H.; Wu, J. Photocatalytic activity of snow-like Bi₂WO₆ microcrystalline for decomposition of Rhodamine B under natural sunlight irradiation. *Mater. Lett.* **2013**, *90*, 107–110. [[CrossRef](#)]
23. Liu, M.; Xue, X.; Yu, S.; Wang, X.; Hu, X.; Tian, H.; Chen, H.; Zheng, W. Improving Photocatalytic Performance from Bi₂WO₆@MoS₂/graphene Hybrids via Gradual Charge Transferred Pathway. *Sci. Rep.* **2017**, *7*, 3637. [[CrossRef](#)]

24. Zhao, S.; Jin, H.; Yang, Y.; Cui, J. Magnetically retrievable Bi₂WO₆/Fe₃O₄/Na-MMT composite: Fabrication and photocatalytic activity. *Res. Chem. Intermed.* **2020**, *46*, 4579–4593. [[CrossRef](#)]
25. Shen, Z.; Li, H.; Hao, H.; Chen, Z.; Hou, H.; Zhang, G.; Bi, J.; Yan, S.; Liu, G.; Gao, W. Novel Tm³⁺ and Yb³⁺ co-doped bismuth tungstate up-conversion photocatalyst with greatly improved photocatalytic properties. *J. Photochem. Photobiol. A Chem.* **2019**, *380*, 111864. [[CrossRef](#)]
26. Liu, Z.; Liu, X.; Wei, L.; Yu, C.; Yi, J.; Ji, H. Regulate the crystal and optoelectronic properties of Bi₂WO₆ nanosheet crystals by Sm³⁺ doping for superior visible-light-driven photocatalytic performance. *Appl. Surf. Sci.* **2020**, *508*, 145309. [[CrossRef](#)]
27. Hou, X.; Liu, J.; Guo, W.; Li, S.; Guo, Y.; Shi, Y.; Zhang, C. A novel 3D-structured flower-like bismuth tungstate/mag-graphene nanoplates composite with excellent visible-light photocatalytic activity for ciprofloxacin degradation. *Catal. Commun.* **2019**, *121*, 27–31. [[CrossRef](#)]
28. Kadeer, K.; Tursun, Y.; Dilinuer, T.; Okitsu, K.; Abulizi, A. Sonochemical preparation and photocatalytic properties of CdS QDs/Bi₂WO₆ 3D heterojunction. *Ceram. Int.* **2018**, *44*, 13797–13805. [[CrossRef](#)]
29. Parnicka, P.; Mikolajczyk, A.; Pinto, H.P.; Lisowski, W.; Klimczuk, T.; Trykowski, G.; Bajorowicz, B.; Zaleska-Medynska, A. Experimental and DFT insights into an eco-friendly photocatalytic system toward environmental remediation and hydrogen generation based on AgInS₂ quantum dots embedded on Bi₂WO₆. *Appl. Surf. Sci.* **2020**, *525*, 146596. [[CrossRef](#)]
30. Ge, L.; Liu, J. Efficient visible light-induced photocatalytic degradation of methyl orange by QDs sensitized CdS-Bi₂WO₆. *Appl. Catal. B Environ.* **2011**, *105*, 289–297. [[CrossRef](#)]
31. Schlaus, A.P.; Spencer, M.S.; Miyata, K.; Liu, F.; Wang, X.; Datta, I.; Lipson, M.; Pan, A.; Zhu, X.Y. How lasing happens in CsPbBr₃ perovskite nanowires. *Nat. Commun.* **2019**, *10*, 265. [[CrossRef](#)]
32. Liu, B.; Feng, S.; Yang, L.; Li, C.; Luo, Z.; Wang, T.; Gong, J. Bifacial passivation of n-silicon metal–insulator–semiconductor photoelectrodes for efficient oxygen and hydrogen evolution reactions. *Energy Environ. Sci.* **2020**, *13*, 221–228. [[CrossRef](#)]
33. Corti, M.; Bonomi, S.; Chiara, R.; Romani, L.; Quadrelli, P.; Malavasi, L. Application of Metal Halide Perovskites as Photocatalysts in Organic Reactions. *Inorganics* **2021**, *9*, 56. [[CrossRef](#)]
34. Zhu, X.; Lin, Y.; San Martin, J.; Sun, Y.; Zhu, D.; Yan, Y. Lead halide perovskites for photocatalytic organic synthesis. *Nat. Commun.* **2019**, *10*, 2843. [[CrossRef](#)] [[PubMed](#)]
35. Cho, S.; Yun, S.H. Structure and optical properties of perovskite-embedded dual-phase microcrystals synthesized by sonochemistry. *Commun. Chem.* **2020**, *3*, 15. [[CrossRef](#)]
36. Mano, G.; Harinee, S.; Sridhar, S.; Ashok, M.; Viswanathan, A. Microwave assisted synthesis of ZnO-PbS heterojunction for degradation of organic pollutants under visible light. *Sci. Rep.* **2020**, *10*, 2224. [[CrossRef](#)]
37. Hu, J.; Yang, M.; Ke, X.; Yang, S.; Wang, K.; Huang, H.; Wang, W.; Luo, D.; Zheng, Z.; Huang, L.; et al. Cubic-cubic perovskite quantum dots/PbS mixed dimensional materials for highly efficient CO₂ reduction. *J. Power Sources* **2021**, *481*, 228838. [[CrossRef](#)]
38. Huang, H.; Zhao, J.; Du, Y.; Zhou, C.; Zhang, M.; Wang, Z.; Weng, Y.; Long, J.; Hofkens, J.; Steele, J.A.; et al. Direct Z-Scheme Heterojunction of Semicoherent FAPbBr₃/Bi₂WO₆ Interface for Photoredox Reaction with Large Driving Force. *ACS Nano* **2020**, *14*, 16689–16697. [[CrossRef](#)]
39. Choi, H.; Stathatos, E.; Dionysiou, D.D. Photocatalytic TiO₂ films and membranes for the development of efficient wastewater treatment and reuse systems. *Desalination* **2007**, *202*, 199–206. [[CrossRef](#)]
40. Lin, R.; Wan, J.; Xiong, Y.; Wu, K.; Cheong, W.C.; Zhou, G.; Wang, D.; Peng, Q.; Chen, C.; Li, Y. Quantitative Study of Charge Carrier Dynamics in Well-Defined WO₃ Nanowires and Nanosheets: Insight into the Crystal Facet Effect in Photocatalysis. *J. Am. Chem. Soc.* **2018**, *140*, 9078–9082. [[CrossRef](#)]
41. Tekin, D.; Tekin, T.; Kiziltas, H. Photocatalytic degradation kinetics of Orange G dye over ZnO and Ag/ZnO thin film catalysts. *Sci. Rep.* **2019**, *9*, 17544. [[CrossRef](#)]
42. Kasinathan, M.; Thiripuranthagan, S.; Sivakumar, A. A facile fabrication of Br-modified g-C₃N₄/rGO composite catalyst for enhanced visible photocatalytic activity towards the degradation of harmful dyes. *Mater. Res. Bull.* **2020**, *130*, 110870. [[CrossRef](#)]
43. Zhang, J.; Fu, X.; Hao, H.; Gan, W. Facile synthesis 3D flower-like Ag@WO₃ nanostructures and applications in solar-light photocatalysis. *J. Alloys Compd.* **2018**, *757*, 134–141. [[CrossRef](#)]
44. Pang, H.-F.; Xiang, X.; Li, Z.-J.; Fu, Y.-Q.; Zu, X.-T. Hydrothermal synthesis and optical properties of hexagonal tungsten oxide nanocrystals assisted by ammonium tartrate. *Phys. Status Solidi* **2012**, *209*, 537–544. [[CrossRef](#)]
45. Bhagyalakshmi, S.B.; Ghimire, S.; Takahashi, K.; Yuyama, K.I.; Takano, Y.; Nakamura, T.; Biju, V. Nonradiative Energy Transfer through Distributed Bands in Piezochemically Synthesized Cesium and Formamidinium Lead Halide Perovskites. *Chemistry* **2020**, *26*, 2133–2137. [[CrossRef](#)]
46. Thorat, A.A.; Dalvi, S.V. Liquid antisolvent precipitation and stabilization of nanoparticles of poorly water soluble drugs in aqueous suspensions: Recent developments and future perspective. *Chem. Eng. J.* **2012**, *181–182*, 1–34. [[CrossRef](#)]
47. Chen, S.; Lu, W.; Shen, H.; Xu, S.; Chen, X.; Xu, T.; Wang, Y.; Chen, Y.; Gu, Y.; Wang, C.; et al. The development of new pigments: Colorful g-C₃N₄-based catalysts for nicotine removal. *Appl. Catal. B Environ.* **2019**, *254*, 500–509. [[CrossRef](#)]
48. Liu, B.; Chen, B.; Zhang, B.; Song, X.; Zeng, G.; Lee, K. Photocatalytic ozonation of offshore produced water by TiO₂ nanotube arrays coupled with UV-LED irradiation. *J. Hazard. Mater.* **2021**, *402*, 123456. [[CrossRef](#)]
49. Woo, O.T.; Chung, W.K.; Wong, K.H.; Chow, A.T.; Wong, P.K. Photocatalytic oxidation of polycyclic aromatic hydrocarbons: Intermediates identification and toxicity testing. *J. Hazard. Mater.* **2009**, *168*, 1192–1199. [[CrossRef](#)] [[PubMed](#)]

50. Vela, N.; Martínez-Menchón, M.; Navarro, G.; Pérez-Lucas, G.; Navarro, S. Removal of polycyclic aromatic hydrocarbons (PAHs) from groundwater by heterogeneous photocatalysis under natural sunlight. *J. Photochem. Photobiol. A Chem.* **2012**, *232*, 32–40. [[CrossRef](#)]
51. Lair, A.; Ferronato, C.; Chovelon, J.-M.; Herrmann, J.-M. Naphthalene degradation in water by heterogeneous photocatalysis: An investigation of the influence of inorganic anions. *J. Photochem. Photobiol. A Chem.* **2008**, *193*, 193–203. [[CrossRef](#)]
52. Benkhennouche-Bouchene, H.; Mahy, J.G.; Wolfs, C.; Vertruyen, B.; Poelman, D.; Eloy, P.; Hermans, S.; Bouhali, M.; Souici, A.; Bourouina-Bacha, S.; et al. Green Synthesis of N/Zr Co-Doped TiO₂ for Photocatalytic Degradation of p-Nitrophenol in Wastewater. *Catalysts* **2021**, *11*, 235. [[CrossRef](#)]
53. Wen, S.; Zhao, J.; Sheng, G.; Fu, J.; Peng, P. Photocatalytic reactions of phenanthrene at TiO₂/water interfaces. *Chemosphere* **2002**, *46*, 871–877. [[CrossRef](#)]
54. Luo, H.; Zeng, Y.; He, D.; Pan, X. Application of iron-based materials in heterogeneous advanced oxidation processes for wastewater treatment: A review. *Chem. Eng. J.* **2021**, *407*, 127191. [[CrossRef](#)]
55. Su, F.; Mathew, S.C.; Lipner, G.; Fu, X.; Antonietti, M.; Blechert, S.; Wang, X. mpg-C₃N₄-Catalyzed Selective Oxidation of Alcohols Using O₂ and Visible Light. *J. Am. Chem. Soc.* **2010**, *132*, 16299–16301. [[CrossRef](#)] [[PubMed](#)]
56. Wu, Z.; Jin, C.; Li, Z.; Yang, D.; Xie, Y.; Wang, M. MoS₂ and g-C₃N₄ nanosheet co-modified Bi₂WO₆ ternary heterostructure catalysts coupling with H₂O₂ for improved visible photocatalytic activity. *Mater. Chem. Phys.* **2019**, *272*, 124982. [[CrossRef](#)]
57. Gong, Y.; Shen, J.; Zhu, Y.; Yan, W.; Zhu, J.; Hou, L.; Xie, D.; Li, C. Tailoring charge transfer in perovskite quantum dots/black phosphorus nanosheets photocatalyst via aromatic molecules. *Appl. Surf. Sci.* **2021**, *545*, 149012. [[CrossRef](#)]